ACS Catalysis

pubs.acs.org/acscatalysis Research Article

Unveiling the Pivotal Role of Ce Coordination Structures and Their Surface Arrangements in Governing 2-Cyanopyridine Hydrolysis for Direct Dimethyl Carbonate Synthesis from CO_2 and Methanol

Linyuan Tian,[▽] Yin-Song Liao,[▽] Zhanping Xiao,[▽] Guohan Sun, Jyh-Pin Chou,* Chun-Yuen Wong, Johnny C. Ho, Yufei Zhao, Pi-Tai Chou,* and Yung-Kang Peng*

Cite This: *ACS Catal.* 2024, 14, 16861−16871 Read Online

ACCESS | Metrics & More | Article Recommendations | Supporting Information

ABSTRACT: The direct synthesis of dimethyl carbonate (DMC) from CO_2 and methanol presents a promising alternative to conventional methods that use toxic chemicals, but its yield is limited by equilibrium. Coupling this reaction with 2-cyanopyridine (2-Cp) hydrolysis over CeO_2-based catalysts was found to significantly boost the DMC yield by removing water. Our recent study has revealed that methanol is the key species being activated by surface Ce sites to produce DMC. The reactivity of surface methoxy species toward CO_2 varies greatly with their configuration, which is determined by the Ce coordination structures. A similar challenge remains in understanding the CeO_2 surface feature governing the hydrolysis of 2-Cp to 2-picolinamide (2-PA). Herein, CeO_2 nanocrystallites with well-defined (111), (110), and (100) surfaces were used to study the effects of Ce coordination structures and their arrangements in this reaction and coupled DMC synthesis. We found that the synergistic adsorption of 2-Cp via cyano-N and pyridine-N on (111) and (110) surfaces enables nucleophilic addition of lattice oxygen, producing imino-like N with stronger Lewis basicity, which in turn facilitates hydrolysis. The (111) surface outperforms the (110) surface due to its unique Ce coordination structure and arrangement, which allows more 2-Cp activation and easier 2-PA desorption. Notably, the (111)-enclosed octahedral CeO_2 used herein outperforms the reported pristine CeO_2 catalysts in this coupled reaction. In contrast, this synergistic adsorption/activation does not occur on the (100) surface, leading to low activity. These findings provide insights for designing CeO_2-based catalysts for CO_2 conversion with alcohols and amines using 2-Cp as a dehydrant.

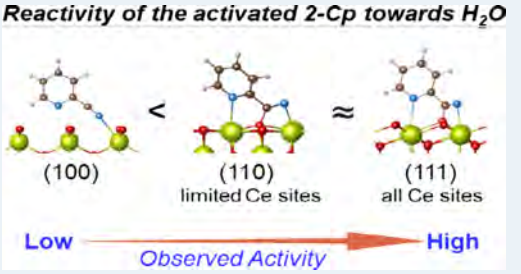

KEYWORDS: *CeO_2, Ce coordination structure, surface atomic arrangement, nitrile hydrolysis, direct dimethyl carbonate synthesis*

INTRODUCTION

Dimethyl carbonate (DMC) is a valuable raw material extensively utilized in solvents, polymer synthesis, fuel/battery additives, and other applications,[1−3] contributing to a global market expected to reach US$ 760 million by 2025.[4] Conventional DMC production methods rely on the use of hazardous and explosive chemicals, such as phosgene and carbon monoxide. To address these concerns, the direct synthesis of DMC by upgrading CO_2 with methanol (reaction (i)) has gained considerable attention due to its environmentally friendly nature.[5] However, the yield of DMC is strongly limited by the thermodynamic equilibrium. To overcome this limitation, water removal techniques such as molecular sieves or organic dehydrants are often employed in conjunction with the reaction to enhance DMC yield.[5] Honda et al., discovered that a tandem carboxylation-hydration reaction catalyzed by CeO_2 can greatly enhance the yield of DMC when combined with nitriles.[6] This intriguing finding revealed that CeO_2, used for direct DMC synthesis, also acts as a catalyst for the hydrolysis of nitriles (reaction (ii)). Among various nitriles, 2-cyanopyridine (2-Cp) was identified as the most effective compound in this coupled reaction and can be regenerated after use. Subsequently, the research interest has mainly focused on the development of CeO_2-based catalysts due to their considerable activity in the coupled reaction, surpassing other common oxide catalysts.[7−9]

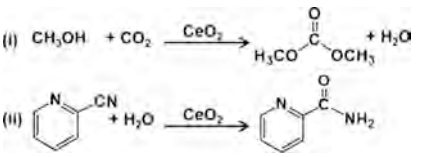

Despite extensive research, the key CeO_2 surface feature that determines the activity in the direct DMC synthesis (reaction (i)) was not disclosed until very recently by our group.[10] The

Received: August 3, 2024
Revised: September 12, 2024
Accepted: October 22, 2024
Published: 0, 2024

https://doi.org/10.1021/acscatal.4c04639
ACS Catal. 2024, 14, 16861−16871

literature often presents discrepancies regarding the influence of Lewis acidity and basicity on DMC yield (Table S1),[11−16] which we attributed to the heavy reliance on NH_3/CO_2-temperature programmed desorption (TPD) for acidity/basicity characterization. The "coordination structure" of active sites is known to be convoluted in a way that affects the measured acidity/basicity in these reports, making simple correlations between these overall properties and catalytic activity insufficient for identifying the key surface feature.[17] Additionally, since NH_3 is not used as a reactant in the reaction, the degree of its desorption from CeO_2 surfaces provides no insights into the atomic interplay between methanol and CeO_2 surfaces. The use of catalysts with poorly defined (or nonuniform) active sites in many studies further increases difficulties in establishing reliable catalytic correlations.[18] We recently addressed this by employing uniform Ce sites enclosed by distinct coordination structures on three common CeO_2 surfaces.[19−21] As shown in Scheme 1a, the Ce

Scheme 1. Illustration of Ce Coordination Structures (with Highlighted Local Geometry of Vacant Orbitals) and Their Arrangements on CeO_2 (a) (111), (b) (110), and (c) (100) Surfaces

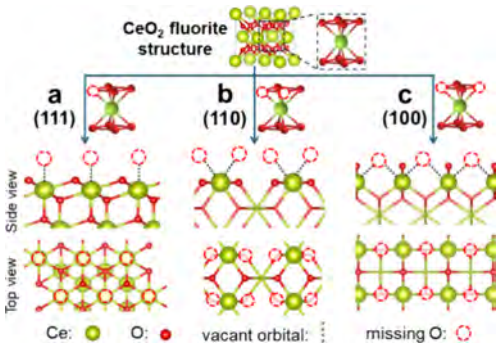

site on the (111) surface is coordinated by seven oxygen atoms with a vacant orbital (from a missing oxygen) oriented perpendicular to the surface plane. In comparison, Ce sites exposed on the (110) (Scheme 1b) and (100) (Scheme 1c) surfaces are coordinated by six oxygen atoms, with the local geometry of vacant orbitals determined by their crystallographic orientation. It is noted that these vacant orbitals (or missing oxygens) are naturally preserved on the pristine CeO_2 surfaces due to the suspension of crystal growth. The coordination structure of the Ce sites associated with these missing oxygens is much more uniform compared to the oxygen vacancy-associated Ce sites often reported in the literature,[22] providing a better platform for in-depth study. Interestingly, we found that the sp^3 oxygen of methanol tends to fill the vacant orbitals on CeO_2 surfaces (cf. the sp^2 oxygen of CO_2), making methanol the key species being activated to produce methyl carbonate and later DMC.[10] The reactivity of the surface methoxy species toward gaseous CO_2 varies considerably, depending on its configuration determined by the geometry of the vacant orbitals on these CeO_2 surfaces.

The hydrolysis of 2-Cp to 2-picolinamide (2-PA, reaction (ii)) presents similar challenges in understanding the key CeO_2 surface feature. For example, Giram et al. correlated a significant decrease in the yield of 2-PA in CeO_2 doped with Al/Cu/Ni/Zr/Zn (cf. pristine CeO_2) to an imbalanced acidity/basicity ratio suggested by NH_3/CO_2-TPD.[16] Conversely, Gupta et al. attributed a 50% increase in activity after doping CeO_2 with Sm/Ru to an optimal acidity/basicity ratio also revealed by NH_3/CO_2-TPD.[23] Other research groups have explored the influence of pristine CeO_2 surfaces on 2-Cp hydrolysis. Using spherical CeO_2 without shape control, Tamura et al. attributed the observed activity to its (111) surface.[24] However, it has been reported that the surface of spherical CeO_2 is rough and comprises not only (111) but also (100) surfaces.[25,26] The Ce sites on these two ill-defined surfaces are expected to demonstrate distinct reactivities compared with their well-defined counterparts. Later, Wang et al. compared CeO_2 crystallites in 2-Cp hydrolysis and found that rod-shaped CeO_2 enclosed by the (110) surface showed superior performance compared to the CeO_2 octahedron (octa.) and cube, exposing (111) and (100) surfaces, respectively.[27] However, the report did not consider the surface area of the CeO_2 crystallites involved in the reaction. Despite the rod's activity being ca. 4 times higher than that of the octa., the surface area of the latter (in microscale) was 30 times smaller than the former (in nanoscale). Additionally, the phosphate stabilizer used in preparing the octahedron was not removed prior to the reaction, which may further suppress the observed activity of this shape.

Herein, surfactant-free CeO_2 nanocrystallites with comparable sizes in the shapes of cube, rod, and octa. enclosed by well-defined (111), (110), and (100) surfaces, respectively, were employed to study the effect of Ce coordination structures and their surface arrangements on the hydrolysis of 2-Cp and the coupled DMC synthesis. The activity of 2-Cp hydrolysis was found to closely correlate with these two factors in the order of (111) > (110) > (100) at all tested temperatures. The adsorption and activation of 2-Cp, as well as the desorption of 2-PA, on these surfaces were carefully investigated with the support of DFT calculations. The synergistic adsorption of 2-Cp, where the cyano-N and pyridine-N coordinate with the CeO_2 surfaces, was identified as the key configuration for the subsequent nucleophilic addition of the lattice oxygen on the (111) and (110) surfaces. This converts the cyano-N into imino-like N with higher Lewis basicity, facilitating the 2-Cp hydrolysis via a pathway distinct from that of the typical pathway on the (100) surface. Although comparable activation energy was obtained for the (111) and (110) surfaces, the high activity of the (111) surface was attributed to its unique Ce coordination structure and arrangement, which enables higher number of 2-Cp activations and easier desorption of 2-PA compared to the (110) surface. The established structure−activity correlation is expected to guide the design of CeO_2-based catalysts for CO_2 conversion with amines and higher alcohols using 2-Cp as a dehydrant.

RESULTS AND DISCUSSION

Catalyst Characterization and Catalytic Testing. Well-defined CeO_2 crystallites in the shapes of cube, rod, and octa. were synthesized using the methods described in previous reports.[19−22] It is noteworthy that the preparation method used for the cube and the rod in this study is similar to the approach employed by Wang et al.[27] However, the octa. prepared in this study is much smaller and does not involve the use of surfactants (Figure S1). The fluorite structure of these samples was first confirmed by X-ray diffraction (XRD) (Figure S2). Their shape and terminal surface were examined using transmission electron microscopy (TEM) (also see Figure S3 for scanning TEM images) and high-resolution TEM

https://doi.org/10.1021/acscatal.4c04639
ACS Catal. 2024, 14, 16861−16871

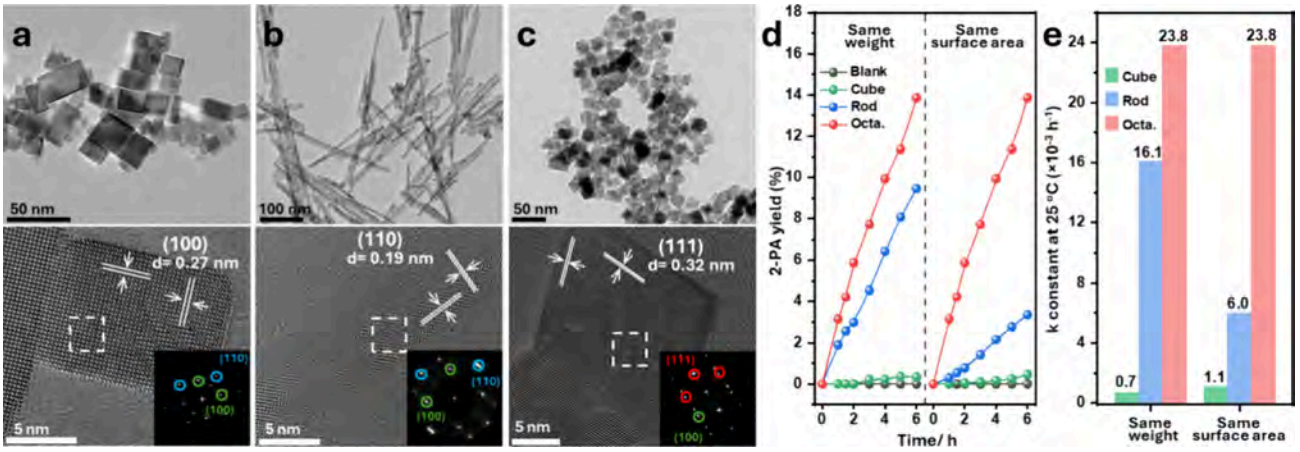

Figure 1. Transmission electron microscope (TEM) images of CeO_2 (a) cube, (b) rod, and (c) octa. and their corresponding high-resolution TEM images (row below). (d) Time-dependent yield of 2-PA in 2-Cp hydrolysis over CeO_2 shapes with equal tested weight (8 mg for each shape) and surface area (10.6 mg for cube, 3.6 mg for rod, and 8 mg for octa.) at room temperature. (e) Corresponding first-order rate constants.

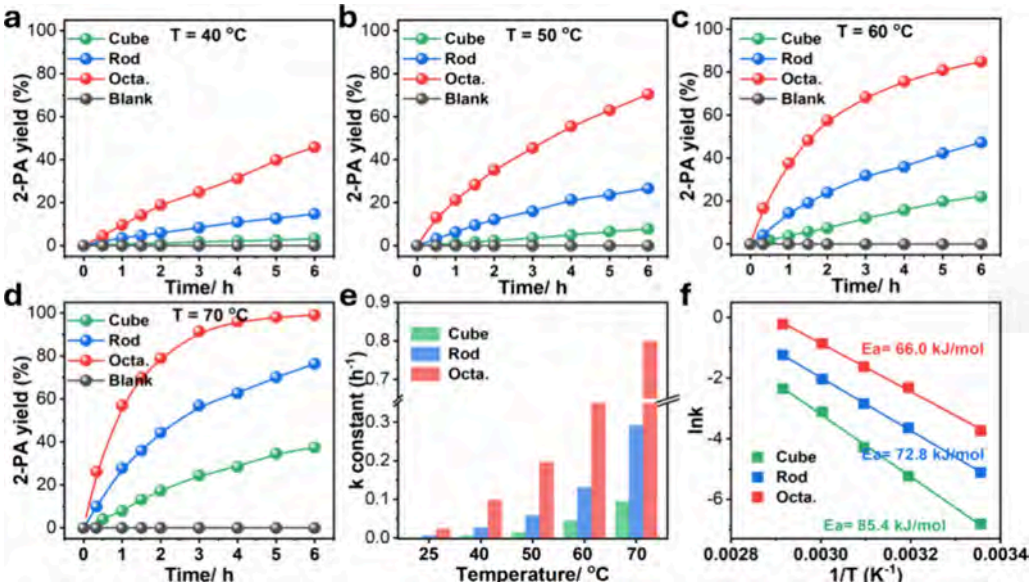

Figure 2. Temperature-dependent yield of 2-PA over CeO_2 shapes with the equal tested surface area at (a) 40, (b) 50, (c) 60, and (d) 70 °C. Comparison of their respective (e) k constant and (f) activation energy.

(HRTEM), respectively. The CeO_2 cube, with a size ranging from 30 to 50 nm, displays a lattice spacing of 0.27 nm, suggesting its (100) termination (Figure 1a). The CeO_2 rod has a diameter of 10 nm and varies in length from 100 to 250 nm. The lateral surface of this sample exhibits a lattice spacing of 0.19 nm, indicating preferential exposure of the (110) surface (Figure 1b). The CeO_2 octa. is about 25 nm in size and primarily exposes the (111) surface, as confirmed by the lattice spacing of 0.32 nm (Figure 1c). Although TEM techniques do not provide information regarding the distribution of facets for each morphology, our recent study using probe-assisted NMR[28−32] showed that these CeO_2 shapes exhibit a facet purity of ≥ 90% (from well-separated ^{31}P peaks) and provide comparable structural uniformity for their hosted Ce sites (from the full width at half-maximum (fwhm)) (Figure S4).[29] Despite several facet distribution models proposed for CeO_2 rods (Figure S5), our recent findings indicate that this morphology is primarily enclosed laterally by the (110) surface, with a small amount of rough (111) surfaces comprised of hydroxylated Ce atoms located at the tips.[21] These Ce atoms are chemically distinct from their counterparts on the well-defined (111) surfaces of CeO_2 octa.[29] The surface areas of the CeO_2 samples are measured in Figure S6, with CeO_2 rod bearing the highest surface area of 95.3 m^2/g, followed by the octa. (43.6 m^2/g), and the cube (32.8 m^2/g). This trend aligns with the crystallite sizes suggested by their XRD peak widths in the order of cube > octa. > rod.

The catalytic activity of the CeO_2 samples in 2-Cp hydrolysis was first investigated at room temperature for 6 h. As shown in Figure 1d, no 2-PA was produced in the absence of CeO_2. When testing the same weight of CeO_2 (8 mg), the octa. exhibits the highest activity, followed by the rod, while the cube displays negligible activity. This trend can be supported by the infrared (IR) spectra of the spent CeO_2 samples, where the octa. exhibits the most prominent 2-PA signals, followed by the rod and cube (Figure S7). It is interesting to see that the 2-Cp cyano group is red-shifted from 2237 to 2218 cm^{-1} on the octa., while such a shift is much smaller for the rod and negligible for the cube. The recyclability of the CeO_2 samples was evaluated over three consecutive cycles (Figure S8). The

https://doi.org/10.1021/acscatal.4c04639
ACS Catal. 2024, 14, 16861−16871

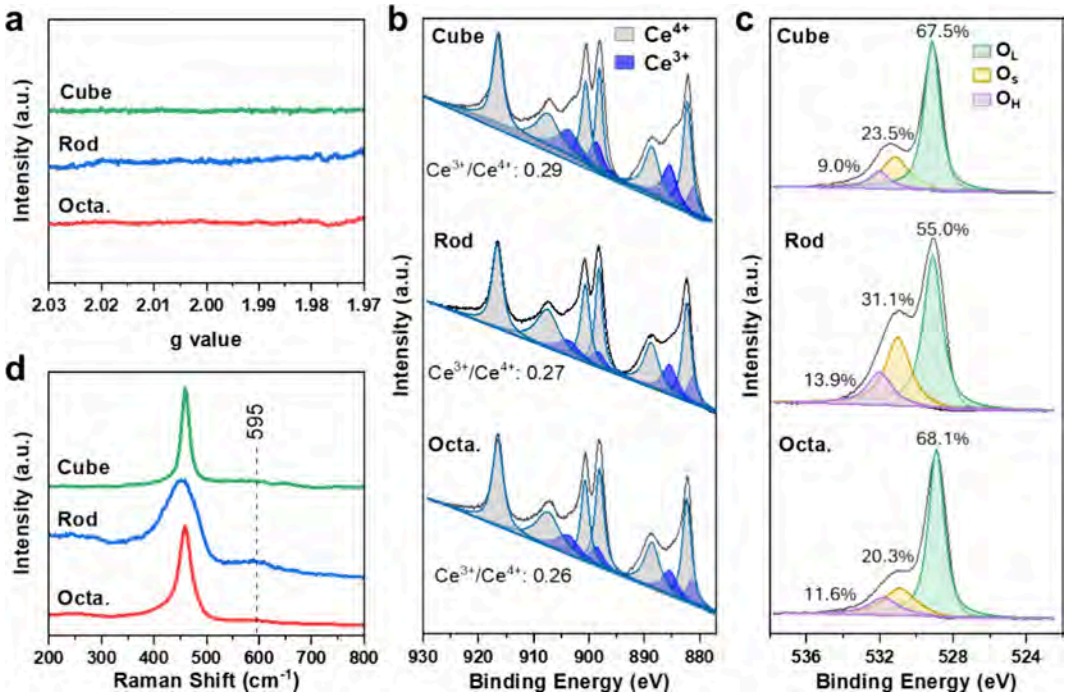

Figure 3. (a) EPR, (b) XPS Ce_{3d}, (c) XPS O_{1s}, and (d) Raman spectra of CeO_2 shapes.

slight decrease in their activity during the second and third rounds can be attributed to catalyst loss during recycling or residual surface-adsorbed 2-Cp/2-PA on the spent catalysts. Both their morphology (Figure S9) and fluorite structure (Figure S10) were maintained throughout the cycles. The rate constant k ($\times 10^{-3}$ h^{-1}) for the first round (Figure 1d) was calculated to be 23.8 for the octa., 16.1 for the rod, and 0.7 for the cube (Figure 1e). No correlation was found between these k constants and their surface area, pore volume, or pore diameter obtained from nitrogen adsorption−desorption isotherms (Figure S6). For example, the octa. has only half the surface area of the rod but demonstrates a higher rate constant k (ca. 1.4 times). Also, the slight difference in the surface area between the octa. (43.6 m^2/g) and the cube (32.8 m^2/g) cannot account for the extreme activity observed in their k constants. These findings suggest that the performance of CeO_2 crystallites is mainly determined by their exposed surfaces (qualitative factor) compared to their corresponding surface areas (quantitative factor). Given ≥90% facet purity for these CeO_2 shapes, we then focused our discussion on their dominant surfaces to simplify the analysis. To evaluate surface activity, CeO_2 samples were further examined under similar total surface areas (i.e., 8 mg for the octa., 3.6 mg for the rod, and 10.6 mg for the cube). As expected, the octa. (111) surface outperforms the other two surfaces (Figure 1d), exhibiting k constants 4 and 22 times higher than that of the rod (110) and cube (100) surfaces, respectively (Figure 1e). A similar trend in activity (Figure 2a−d) and k constants (Figure 2e, see kinetic plots in Figure S11) can also be observed for these samples at elevated temperatures from 40 to 70 °C. Although the rod sample in this study comprises a (ca. 10%) rough (111) surface with hydroxylated Ce atoms, their contribution to the activity is considered negligible due to steric hindrance from surface hydroxyl groups affecting 2-Cp adsorption/activation (vide infra). The activation energy (E_A) of CeO_2 surfaces was calculated to be 85.4 kJ/mol for the cube (100) surface, 72.8 kJ/mol for the rod (110) surface, and 66.0 kJ/mol for the octa. (111) surface (Figure 2f). Altogether, we demonstrate that 2-Cp can be activated very differently among CeO_2 surfaces, and the (111) surface is the most active surface rather than the previously reported (110) surface. However, in our opinion, the small difference in their E_A may not fully explain the large difference observed in their surface activities (Figure 2e). It is likely that some other factors collectively contribute to the observed activity.

Overall properties such as oxygen vacancies, Ce^{3+}/Ce^{4+} ratio, hydroxyl groups, and Lewis acidity/basicity on the catalysts' surface have often been utilized in the literature to account for differences in the observed activity.[33,34] Electron paramagnetic resonance (EPR) was first employed to confirm the absence/presence of surface oxygen vacancies, as the signal at g = 2.00 is typically associated with unpaired electrons trapped in surface oxygen vacancies by adsorbed O_2.[35] The absence of this signal in the CeO_2 shapes suggests that the contribution of surface oxygen vacancies to their activity is negligible (Figure 3a). This finding is also supported by their similar X-ray photoelectron spectroscopy (XPS) Ce_{3d} spectra with comparable Ce^{3+}/Ce^{4+} ratios (Figure 3b). Bear in mind that the surface oxygen vacancies typically mentioned in the literature are distinct from the missing oxygens preserved on the pristine CeO_2 surfaces here (Scheme 1).[22] The XPS O_{1s} spectra of all the CeO_2 shapes (Figure 3c) show a prominent peak corresponding to lattice oxygens (O_L) at around 529.5 eV, along with a shoulder peak deconvoluted into surface oxygen species (O_S) at ca. 531 eV and surface hydroxyl groups (O_H) at ca. 532 eV.[36] Given the absence of the surface oxygen vacancies revealed above, it is more likely that the surface coordination unsaturated oxygen atoms are the main contributor to O_S in these CeO_2 shapes, as supported by the correlation between its intensity and their BET surface areas. Considering that (1) the octa. and cube, which exhibit opposing activity, possess similar amounts of O_S and O_H and (2) the rod, which has the highest amount of O_S and O_H, only exhibit medium activity, these two surface species should thus

https://doi.org/10.1021/acscatal.4c04639
ACS Catal. 2024, 14, 16861−16871

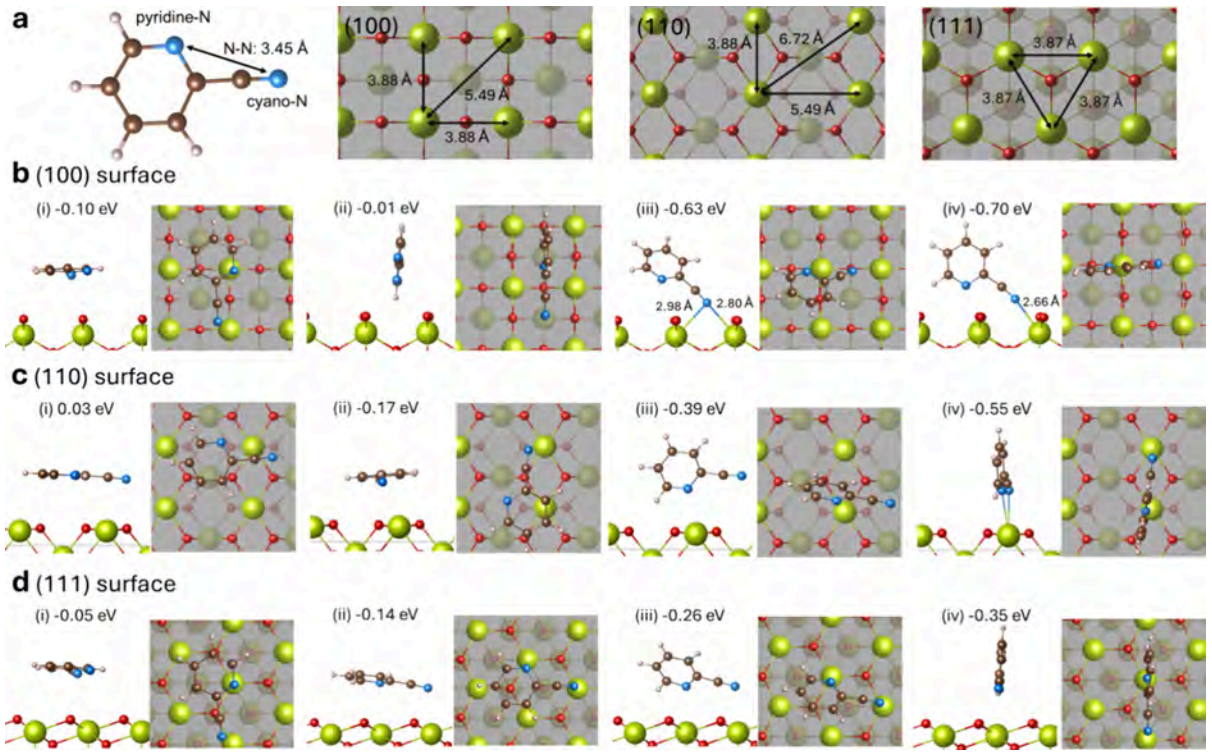

Figure 4. (a) Analysis of distances between N atoms in 2-Cp and Ce sites on CeO_2 surfaces. The adsorption configuration and energy of 2-Cp on (b) (100), (c) (110), and (d) (111) surfaces with side (left) and top (right) views.

play a negligible role in influencing the activity of the CeO_2 shapes (Figure 2). This crystallite size-dependent property is also evident in their Raman spectra (Figure 3d), where the rod sample exhibits a significantly broader F_{2g} peak at ~452 cm^{-1} (cf. the cube and octa.) and is accompanied by a tiny LO mode (Raman inactive) located at 595 cm^{-1}. This suggests that the rod, which has the highest surface area, contains a greater proportion of surface or subsurface oxygen atoms in the $Ce-O_{8-x}$ units, which are stretched in a less symmetric manner relative to the bulk oxygen atoms in the $Ce-O_8$ units.[37] Regarding the Lewis acidity/basicity of CeO_2 shapes revealed by NH_3/CO_2-TPD (Figure S12), we found no correlation with their activity in this reaction likely due to the convolution of Ce coordination structures, as discussed in the Introduction. Altogether, these overall properties often used in the literature for catalytic correlation fail to explain the differences in activity even for catalysts as simple as pristine CeO_2 here.

Insights from Density Functional Theory (DFT) Calculations. The atomic arrangement and coordination structure of the Ce sites on the CeO_2 surfaces have been demonstrated to have a profound influence on regulating not only the adsorption and activation of reactants but also the desorption of products.[19−22] In this study, 2-Cp is believed to adsorb on the CeO_2 surfaces through the interaction between its pyridine-N/cyano-N atoms and the vacant orbital(s) of surface Ce sites (Scheme 1). The distance between the pyridine-N and cyano-N atoms in 2-Cp (3.45 Å) is close to the shortest Ce−Ce distance (3.87−3.88 Å) on the CeO_2 surfaces (Figure 4a), suggesting that they may also synergistically facilitate the adsorption of 2-Cp. DFT calculations were employed to provide atomic insights into this adsorption process. On the (100) surface (Figure 4b), no synergistic effect was observed between the pyridine-N and cyano-N atoms of 2-Cp during adsorption. Instead, its adsorption configuration was primarily dictated by the geometry of the vacant orbitals on the surface, where the cyano-N atom tends to fill the missing oxygen site, leading to adsorption energies (E_{ad}) of −0.63 eV for (Figure 4b(iii)) and −0.70 eV for (Figure 4b(iv)). Interestingly, the pyridine-N atom, which has stronger Lewis basicity compared to the cyano-N, was not able to interact with Ce sites on this surface, likely due to the mismatch in their orbitals and the steric hindrance effect from the cyano group. A different adsorption behavior of 2-Cp was observed on the (110) surface, (Figure 4c). The cyano-N and pyridine-N can independently interact with the surface Ce sites along their vacant orbitals (with a slight tilt), but these individual interactions are relatively weak with an E_{ad} of −0.17 eV (Figure 4c(ii)) and −0.39 eV (Figure 4c(iii)), respectively. A synergistic 2-Cp adsorption mediated by both the cyano-N and pyridine-N was observed on the Ce sites that are close next to each other at a distance of 3.88 Å, resulting in the most negative E_{ad} of −0.55 eV on this surface (Figure 4c(iv)). No such synergistic 2-Cp adsorption can be seen for the Ce sites that are further apart in distances of 5.49 and 6.72 Å on the (110) surface (Figure 4a). Interestingly, all the 2-Cp adsorption cases on the (111) surface were mediated by both the cyano-N and pyridine-N (Figure 4d) with E_{ad} increasing from −0.14 eV in a flat configuration (Figure 4d(ii)) to a more negative value of −0.35 eV in a stand-up configuration (Figure 4d(iv)). We attributed this to the unique arrangement and coordination structure of the Ce sites on this surface, where all the Ce sites with vacant orbitals perpendicular to the surface plane are situated at a distance close to the distance between the pyridine-N and cyano-N atoms in 2-Cp. These findings highlight the critical role of the surface atomic arrangement and coordination structure of the

https://doi.org/10.1021/acscatal.4c04639
ACS Catal. 2024, 14, 16861−16871

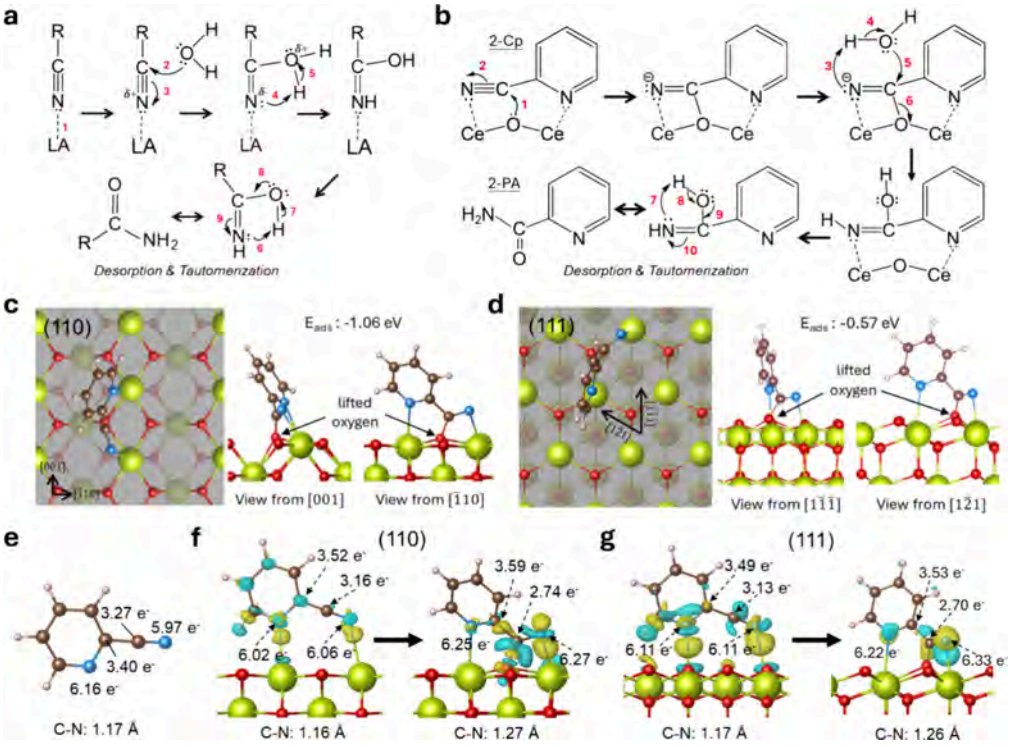

Figure 5. (a) Typical Lewis acid-catalyzed nitrile hydrolysis and (b) proposed activation of the adsorbed 2-Cp by CeO_2 and its facilitated hydrolysis. The nucleophilic addition of the surface $O_{lattice}$ to the cyano-C atom of adsorbed 2-Cp on (c) (110) and (d) (111) surfaces. The Bader charge analysis of (e) 2-Cp and the adsorbed 2-Cp before and after activation on (f) (110) and (g) (111) surfaces.

Ce sites in collectively affecting the adsorption behavior of 2-Cp on the CeO_2 surfaces.

Interestingly, the trend in E_{ad} obtained for 2-Cp on these CeO_2 surfaces (i.e., (100) > (110) > (111)) is opposite to their activity (i.e., (111) > (110) > (100)), suggesting that the adsorption of 2-Cp is not the key step leading to observed activity. As is known, a strong adsorption of a reactant without being effectively activated could even poison the active site. Distinct from the typical Lewis acid-catalyzed mechanism (Figure 5a), Tamura et al.[38] proposed that the nucleophilic addition of CeO_2 surface lattice oxygen ($O_{lattice}$) to the cyano-C atom of the adsorbed 2-Cp can convert cyano-N into a negatively charged imino-like N (Figure 5b). This imino-like N is believed to facilitate 2-Cp hydrolysis by deprotonating H_2O to form a hydroxide with a stronger Lewis basicity (cf. H_2O in Figure 5a). A similar mechanism was also proposed by Sawabe et al.[39] To examine this pathway on CeO_2 surfaces, the strength of the Ce−$O_{lattice}$ bonds on the CeO_2 surfaces was further analyzed using the crystal orbital Hamilton population (COHP) method (see the experimental section for details).[40] This approach allows us to quantitatively assess the ease of lifting the surface $O_{lattice}$ in the proposed nucleophilic addition step. The integrated COHP (ICOHP) values indicate the magnitude of the bond strength; to make these values more intuitive, ICOHP was represented as -ICOHP here, where higher ICOHP values indicate stronger bond strength. As shown in Figure S13, the (100) surface exhibits the highest Ce−$O_{lattice}$ bond strength of 3.88 eV, followed by 3.03 eV for the (110) surface and 2.94 eV for the (111) surface. This result suggests that the difficulty of lifting surface $O_{lattice}$ for nucleophilic addition is in the trend of (100) > (110) > (111), which is in a good correlation with their E_A obtained in Figure 2f (see Figure S14).

We then examined the proposed activation pathway of adsorbed 2-Cp on CeO_2 surfaces using their adsorption configurations with the most negative E_{ad}. The nucleophilic addition of the surface $O_{lattice}$ on the cyano-C atom of the adsorbed 2-Cp was not successful on the (100) surface, likely due to the long distance between them (Figure 4b(iv)) and the high energy required to lift the surface $O_{lattice}$. For the (110) surface, the surface $O_{lattice}$ is able to undergo nucleophilic addition to the cyano-C atom of adsorbed 2-Cp in the configuration shown in Figure 4c(iv). Given the limited distance for the surface to lift the $O_{lattice}$, the activated 2-Cp exhibits a tilted configuration on this surface with the E_{ad} nearly doubled to −1.06 eV (Figure 5c). However, such a tilted configuration is believed to impose steric hindrance to the activation of other 2-Cp sitting on Ce sites in the next row, limiting the number of 2-Cp being effectively activated. The activation of adsorbed 2-Cp is also allowed on the (111) surface for the configuration shown in Figure 4d(iv). In contrast, activated 2-Cp was found to remain in a stand-up configuration with E_{ad} slightly increased to −0.57 eV (Figure 5d). Such a stand-up activated configuration of 2-Cp, together with the closely packed Ce sites on the (111) surface, allows for the activation of a higher number of 2-Cp compared to the (110) surface. However, it was observed that the synergistic adsorption of 2-Cp is thermodynamically unfavorable on the 25% hydroxylated (111) surface (Figure S15), suggesting that the contribution of hydroxylated Ce atoms on the rough (111) surface to the rods' activity is very limited. Consequently, the observed activity of the rod sample should primarily originate from its lateral (110) surface in this reaction. We further analyzed the Bader charge of the pyridine-N, pyridine-C, cyano-C, and cyano-N atoms in pristine 2-Cp (Figure 5e) and its adsorption on the (110) (Figure 5f) and (111) (Figure 5g)

https://doi.org/10.1021/acscatal.4c04639
ACS Catal. 2024, 14, 16861−16871

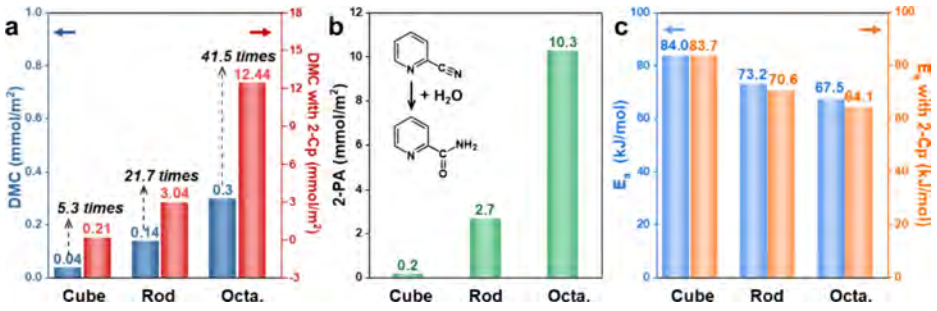

Figure 6. (a) Direct DMC synthesis catalyzed by CeO_2 shapes in the absence/presence of 2-Cp at 140 °C, (b) production of 2-PA during the direct DMC synthesis with 2-Cp, and (c) corresponding E_A.

surfaces before/after activation (i.e., nucleophilic addition by $O_{lattice}$). The results show that the pyridine-N and pyridine-C experience a minor change in Bader charge (<0.2 e^-) during the adsorption and activation of 2-Cp. In contrast, the Bader charge of the cyano-C decreases significantly from around 3.2 e^- for the pristine/adsorbed 2-Cp to about 2.7 e^- after being nucleophilically attacked by the $O_{lattice}$ on both the (110) and (111) surfaces. Such activation of 2-Cp not only makes the cyano-C more acidic for the subsequent nucleophilic addition of H_2O/hydroxides (step 5 in Figure 5b) but also induces an increase in the Bader charge of the cyano-N from around 6.0 e^- for the pristine/adsorbed 2-Cp to about 6.3 e^-. The accompanied weakening of the C≡N triple bond can be evidenced by the bond lengthening from 1.16 to 1.17 Å for the pristine and the adsorbed 2-Cp to 1.26−1.27 Å after the nucleophilic addition of the $O_{lattice}$ (the bond length for the C═N double bond is 1.37 Å). This is experimentally supported by the red shift of the 2-Cp cyano (C≡N) signal from 2237 to 2218 cm^{-1} in the IR spectra of the octa. and rod (Figure S7). The extent of this shift is closely related to the number of successfully activated 2-Cp molecules with the octa. showing a higher population than that of the rod. Since nucleophilic addition of $O_{lattice}$ is hindered on the (100) surface, no such shift can be observed for the cube. All these findings suggest that the activation of the adsorbed 2-Cp can be facilitated via the proposed pathway on both the (110) and (111) surfaces, with the (111) surface exhibiting more effective activations owing to its unique Ce coordination structure and surface arrangement.

In addition to the adsorption (Figure 4) and activation (Figure 5) of 2-Cp, the desorption of the product, 2-PA, from the (110) and (111) surfaces was also studied, as this step may affect the regeneration of the Ce sites and hence the observed surface activity. As shown in Figure S16, the E_{ad} of 2-PA on the (110) surface (−0.87 eV) is nearly twice as high as that on the (111) surface (−0.46 eV), with an extra hydrogen bond formation between the surface $O_{lattice}$ and the H atom of 2-PA on the (110) surface. The desorption of 2-PA from the (110) surface is thus expected to be slower than that from the (111) surface. However, this desorption step alone may not account for the significant difference in their observed activity (Figure 2e) at a close E_A (Figure 2f). We have correlated the comparable E_A obtained for these two surfaces to their barrier required to undergo the alternative activation pathway (Figure S14). Given this, the observed activity should be closely related to the number of activated 2-Cp molecules via the pathway, wherein a synergistic 2-Cp adsorption mediated by both cyano-N and pyridine-N is required. Since all Ce sites on the (111) surface can participate in the synergistic 2-Cp adsorption and activation w/o steric hindrance compared to their counterparts on the (110) surface (Figure 4), this should collectively explain the significant difference in activity observed between the octa. and the rod. The negligible activity of the cube (100) surface in 2-Cp hydrolysis at room temperature can be attributed to the high E_A of the traditional Lewis acid-catalyzed pathway (Figure 5a). We further confirmed this point on the octa. by replacing 2-Cp with benzonitrile and compounds with their cyano-N and pyridine-N in the *meta* (i.e., 3-Cp) and *para* (i.e., 4-Cp) positions. As expected, no synergistic adsorption configuration can be seen for them on the (111) surface (Figure S17), and no hydrolysis of these molecules was observed on the octa. at room temperature (Table S2).

Direct DMC Synthesis Coupled with 2-Cp Hydrolysis. The impact of 2-Cp as a dehydrant in the direct DMC synthesis was further explored over these CeO_2 shapes to demonstrate the critical role of Ce coordination structures and their arrangements in the coupled reaction. In the absence of 2-Cp (blue column, Figure 6a), the production of DMC in three hours was 0.3 mmol/m^2 for the octa., which is two times and seven times higher than that of the rod (0.14 mmol/m^2) and the cube (0.04 mmol/m^2), respectively. In our previous report,[10] the difference in their DMC activity was attributed to the formation of surface methoxy species with varying reactivities toward CO_2. When 2-Cp was added (red column, Figure 6a), a notable enhancement in the DMC yield can be observed for CeO_2 shapes within the same period of time. The octa. showed a 41.5-fold increase in DMC yield to 12.44 mmol/m^2, followed by 21.7-fold and 5.3-fold increases for the rod (to 3.04 mmol/m^2) and the cube (to 0.21 mmol/m^2), respectively. Surprisingly, the DMC yield of the octa. w/o 2-Cp concentration (0.3 mmol/m^2) was even higher than that of the cube with 2-Cp (0.21 mmol/m^2), highlighting the importance of surface understanding and control in this coupled reaction. The added 2-Cp was found to remove H_2O produced from the direct DMC synthesis in a nearly one-to-one manner, as evidenced by the similar amount of 2-PA yield (cf. DMC) for CeO_2 shapes (Figure 6b). This, together with their maintained E_A in the absence/presence of 2-Cp (Figure 6c, also see Figure S18), suggests that the substantial increase in DMC yield observed for the octa. is due to the effective hydrolysis of 2-Cp by the (111) surface, which greatly drives the equilibrium to the product side. The DMC activity of the CeO_2 shapes was further compared with those of pristine CeO_2 catalysts reported in the literature. In the absence of a dehydrant (Table S3), many of these catalysts outperform the octa. in terms of the DMC formation rate (mmol/g/h), likely due to their higher surface area. However, when a dehydrant is

https://doi.org/10.1021/acscatal.4c04639
ACS Catal. 2024, 14, 16861−16871

Table 1. Comparison of DMC Activity among Pristine CeO_2 Catalysts (in the Presence of a Dehydrant) Reported in the Literature[a]

entry	CeO_2 shapes	surface area (m^2/g)	amount (g)	amount of MeOH (mmol)	CO_2 pressure (MPa)	dehydrant agent (mmol)	temp. (K)	time (h)	DMC amount (mmol)	DMC rate (mmol/g/h)	ref
1	sphere	80	0.17	200	0.5	CH_3CN (600)	423	2	2	5.9	41
2	sphere	80	0.17	100	0.5	PhCN (300)	423	2	4.7	14	42
3	sphere	80	0.01	200	5	2-Cp (10)	393	0−2	0.5−2.0	75	43
4	rod	n.r.	0.1	370	5	2-Cp (50)	413	3	37.8	126	27
5	octa.	n.r.	0.1	370	5	2-Cp (50)	413	3	6.6	22	27
6	cube	n.r.	0.1	370	5	2-Cp (50)	413	3	0.96	3.2	27
7	sphere	n.r.	0.1	370	5	2-Cp (50)	413	3	35	116	27
8	sphere	77	0.1	100	5	2-Cp (50)	423	2	15.8	79	44
9	cube	43	0.1	100	5	2-Cp (50)	423	2	15.7	79	44
10	rod	105	0.1	100	5	2-Cp (50)	423	2	17.7	89	44
11	spindle	36	0.1	100	5	2-Cp (50)	423	2	30.5	150	44
12	spindle	n.r.	0.1	370	5	DMP (29)	413	2	2.8	14	45
13	octa.	n.r.	0.1	370	5	DMP (29)	413	2	0.83	4.2	45
14	cube	n.r.	0.1	370	5	DMP (29)	413	2	0.28	1.4	45
15	cube	32.8	0.05	370	4	2-Cp (50)	413	3	0.344	2.296	this work
16	rod	95.3	0.05	370	4	2-Cp (50)	413	3	14.48	96.57	this work
17	octa.	43.6	0.05	370	4	2-Cp (50)	413	3	27.12	180.79	this work

[a]The "Sphere" symbol used in the column of the "CeO_2 shape" represents catalysts without shape control.

added (Table 1), the octa., which has a relatively low surface area, exhibits the highest DMC formation rate reported among pristine CeO_2 catalysts to date.[27,41−45] This indicates that the hydrolysis of nitrile (reaction (ii)) is more surface-sensitive compared to direct DMC synthesis (reaction (i)) in the coupled reaction, underscoring the significance of surface control even for pristine catalysts.

CONCLUSIONS

In summary, this work has unraveled the pivotal influence that the "coordination structures" and "arrangements" of Ce sites on CeO_2 (100), (110), and (111) surfaces exert on the hydrolysis of 2-Cp. The kinetic studies revealed that the rate constant for 2-Cp hydrolysis is surface-dependent, with the (111) surface exhibiting the highest catalytic activity, followed by the (110) surface, while the (100) surface displays negligible activity at room temperature. Overall properties such as oxygen vacancies, the Ce^{3+}/Ce^{4+} ratio, and hydroxyl groups were found to be comparable among these surfaces and hence fail to account for the observed differences in their activity. DFT calculations suggest that the synergistic adsorption of 2-Cp via its cyano-N and pyridine-N on the (110) and (111) surfaces is the key configuration for the later nucleophilic addition of the $O_{lattice}$, which produces acidic cyano-C and imino-like N collectively facilitating 2-Cp hydrolysis via the proposed pathway. Although the E_A required for this process is comparable for these two surfaces, the (111) surface allows more effective activations due to its unique Ce coordination structure and surface arrangement. This, together with the higher 2-PA desorption energy required for the (110) surface, explains why the (111) surface can display significantly higher activity in 2-Cp hydrolysis and coupled DMC synthesis. The (111)-enclosed octahedral CeO_2 was even found to outperform all pristine CeO_2 catalysts reported to date in this coupled reaction. The absence of synergistic 2-Cp adsorption on the (100) surface and the high E_A required for the typical activation pathway result in low activity in both 2-Cp hydrolysis and the coupled DMC synthesis. The atomic insights revealed in this study should guide the design and synthesis of CeO_2-based catalysts in 2-Cp hydrolysis to couple with not only CO_2 conversion with methanol but also higher alcohols and amines into valuable (poly)carbonates, ureas, and carbamates (Figure S19).

METHODS

Catalyst Preparation. The CeO_2 shapes were synthesized following previously reported methods.[19−21] For the cube, 0.651 g of $Ce(NO_3)_3{\cdot}6H_2O$ and 3.6 g of NaOH were mixed with 30 mL of water and stirred for 30 min. To prepare the rod, the same procedure was used but with an increased amount of NaOH (7.2 g). The resulting mixtures were then transferred to Teflon-lined stainless-steel containers and heated at 180 °C for the cube and 100 °C for the rod, both for 24 h. For the octa., 0.8141 g of $Ce(NO_3)_3{\cdot}6H_2O$ and 0.7005 g of hexamethylenetetramine (HMT) were added to 110 mL of water and stirred for 3 h at 75 °C. All catalysts were collected by centrifugation, washed three times with ethanol, and then calcined/dried in air at 200 °C before use.

Catalyst Characterization. XRD using a D2 PHASER second generation Bruker instrument with monochromatized Cu Kα radiation was employed to identify the crystalline phases of CeO_2. The material morphology was investigated using a Philips Technai TEM. HRTEM images were obtained with a JEOL 1200F microscope operating at an acceleration voltage of 200 kV to observe the lattice spacing of the CeO_2 samples. XPS data were recorded on a Thermo Scientific Nexsa system (12 kV, 6 mA), with binding energies calibrated using the C_{1s} peak at 284.8 eV. Nitrogen adsorption−desorption isotherms for the CeO_2 samples were measured at 77 K using a Micromeritics ASAP 2460 instrument. Infrared and Raman spectroscopies were conducted with Perkin−Elmer Spectrum 100 and Bayspec Agility (785 nm), respectively. EPR measurements were performed at ambient temperature using an ADANI SpinscanX spectrometer, operating at a 100 kHz

https://doi.org/10.1021/acscatal.4c04639
ACS Catal. 2024, 14, 16861−16871

field modulation with a modulation amplitude of 150 microtesla (μT).

2-Cp Hydrolysis. The hydrolysis of 2-Cp (to 2-PA) was assessed using CeO_2 samples as follows: 1 mmol of 2-Cp and 8 mg of CeO_2 were added to 5 mL of H_2O to initiate the reaction. At each time point, the solution was centrifuged at 12,000 rpm for 8 min to separate CeO_2, followed by product analysis using GC-MS (Agilent 5890, column: 30 m × 0.25 mm × 0.25 μm) and GC (Agilent 6890, column: TG-5SilMS, 30 m × 0.25 mm × 0.25 μm). The concentration of the target product in the solution was determined by integrating the area of its peak and comparing it with commercial reference standards. The conversion at each time point was calculated based the equation below:

$$\text{Conversion} = \frac{\text{moles of 2 - PA}}{\text{initial moles of 2 - Cp}} \times 100\%$$

The activation energy for CeO_2 samples in this reaction was calculated by the Arrhenius equation concerning the dependence of the rate constant of a chemical reaction on the absolute temperature as

$$\ln k = -\frac{E_a}{RT} + \ln A$$

where k is the rate constant (frequency of collisions resulting in a reaction); T is the absolute temperature; A is the pre-exponential factor or Arrhenius factor or frequency factor; E_a is the molar activation energy for the reaction; and R is the universal gas constant.

DMC Synthesis. The direct DMC synthesis from CO_2 and methanol was performed in an autoclave. In a typical experiment, the autoclave was charged with 15 mL of methanol, 50 mmol of 2-Cp, and 50 mg of the catalyst. It was then purged with CO_2 five times to remove air before being pressurized with CO_2 to 4 MPa and heated to 140 °C for 3 h. After the reaction, the solution was centrifuged at 12,000 rpm to separate CeO_2, and the products were analyzed using GC-MS. For the DMC synthesis without a dehydrant, the same reaction conditions were applied, excluding the addition of 2-Cp. To evaluate the activation energy for the CeO_2 samples with and without 2-Cp, reactions were carried out at temperatures ranging from 120 to 180 °C for 30 min to obtain the initial reaction rates for use in the Arrhenius equation described above.

Computational Details. Density functional theory (DFT) calculations were performed using the Vienna ab initio simulation package (VASP),[46] which employs plane-wave basis sets to expand electronic wave functions. The projected-augmented wave (PAW)[47,48] method was utilized to describe the valence-core electronic interactions, with a cutoff energy of 460 eV. It is well-known that the (semi)local functional, such as general gradient approximation (GGA),[49] would fail to accurately describe the electronic structure of systems with strongly correlated electrons occupying f-orbitals. To address this issue, the on-site DFT+U proposed by Dudarev et al. was implemented, with a U value of 3.5 eV.[50] The optimized primitive lattice constant of CeO_2 was found to be 3.88 Å. Five-layered (100), (110), and (111) CeO_2 surface slabs were constructed, with the bottom three layers fixed and the top two layers allowed to relax. To ensure comparable coverage of different adsorbates, the surface supercell models (100)-4 × 4, (110)-3 × 4, and (111)-4 × $2\sqrt{3}$-$R30°$ with areas of 2.41, 2.56, and 2.07 nm^2, respectively, were considered. The k-points of 2 × 2 × 1 were used to sample the Brillouin zone for three models. To eliminate the fictitious interactions between periodic images, a 20 Å-thick vacuum slab was built into surface models. The adsorption energy (E_{ads}) was calculated using the equation: $E_{ads} = E_{total} - E_{surface} - E_{molecule}$, where E_{total}, $E_{surface}$, and $E_{molecule}$ represent the total energy of the system, the energy of the pristine surface, and the energy of the adsorbate (e.g., 2-Cp, 3-Cp, and 4-Cp, benzonitrile, and nicotinamide), respectively. To analyze the bond strength of surface Ce−O, we employed the integrated crystal orbital Hamiltonian populations (ICOHP) through LOBSTER,[40] which directly extract chemical bonding information from DFT calculations. This approach provides insights into the bonding/antibonding interactions by partitioning the electronic density of states into bonding, nonbonding, and antibonding contributions.

■ ASSOCIATED CONTENT

Supporting Information

The Supporting Information is available free of charge at https://pubs.acs.org/doi/10.1021/acscatal.4c04639.

Characterization and catalytic testing of CeO_2 shapes (TGA, XRD, STEM, ^{31}P NMR, BET, FTIR) and DFT calculations of 2-Cp/2-PA molecules on CeO_2 surfaces

■ AUTHOR INFORMATION

Corresponding Authors

Jyh-Pin Chou − *Graduate School of Advanced Technology, National Taiwan University, Taipei 106319, Taiwan;* orcid.org/0000-0001-8336-6793; Email: jpchou@ntu.edu.tw

Pi-Tai Chou − *Department of Chemistry, National Taiwan University, Taipei 106319, Taiwan;* orcid.org/0000-0002-8925-7747; Email: chop@ntu.edu.tw

Yung-Kang Peng − *Department of Chemistry, City University of Hong Kong, Hong Kong 999077, Hong Kong SAR;* orcid.org/0000-0001-9590-6902; Email: ykpeng@cityu.edu.hk

Authors

Linyuan Tian − *Department of Chemistry, City University of Hong Kong, Hong Kong 999077, Hong Kong SAR*

Yin-Song Liao − *Tsing Hua Interdisciplinary Program, National Tsing Hua University, Hsinchu 300, Taiwan*

Zhanping Xiao − *Department of Chemistry, City University of Hong Kong, Hong Kong 999077, Hong Kong SAR; Department of Chemistry, National Taiwan University, Taipei 106319, Taiwan*

Guohan Sun − *Department of Chemistry, City University of Hong Kong, Hong Kong 999077, Hong Kong SAR*

Chun-Yuen Wong − *Department of Chemistry, City University of Hong Kong, Hong Kong 999077, Hong Kong SAR;* orcid.org/0000-0003-4780-480X

Johnny C. Ho − *Department of Materials Science and Engineering, City University of Hong Kong, Hong Kong 999077, Hong Kong SAR;* orcid.org/0000-0003-3000-8794

Yufei Zhao − *State Key Laboratory of Chemical Resource Engineering, Beijing University of Chemical Technology, Beijing 100029, China;* orcid.org/0000-0002-5325-8991

Complete contact information is available at:

https://doi.org/10.1021/acscatal.4c04639
ACS Catal. 2024, 14, 16861−16871

https://pubs.acs.org/10.1021/acscatal.4c04639

Author Contributions

[▽]L.T., Y.-S.L., and Z.X. contributed equally to this work

Notes

The authors declare no competing financial interest.

■ ACKNOWLEDGMENTS

The authors would like to thank the financial support from the Hong Kong Research Grants Council (CityU 11300020 and CityU 11305721) and the Strategic Interdisciplinary Research Grant of City University of Hong Kong (project no. 7020053).

■ REFERENCES

(1) Kim, K. H.; Lee, E. Y. Environmentally-benign dimethyl carbonate-mediated production of chemicals and biofuels from renewable bio-oil. *Energies* **2017**, *10*, 1790.
(2) Tan, H.-Z.; Wang, Z.-Q.; Xu, Z.-N.; Sun, J.; Xu, Y.-P.; Chen, Q.-S.; Chen, Y.; Guo, G.-C. Review on the synthesis of dimethyl carbonate. *Catal. Today* **2018**, *316*, 2−12.
(3) Fiorani, G.; Perosa, A.; Selva, M. Dimethyl carbonate: a versatile reagent for a sustainable valorization of renewables. *Green Chem.* **2018**, *20*, 288−322.
(4) Global Dimethyl Carbonate Market 2017−2025 (February 12, 2018). https://www.businesswire.com/news/home/20180212005686/en/Global-Dimethyl-Carbonate-Market-2017-2025.
(5) Shi, D.; Heyte, S.; Capron, M.; Paul, S. Catalytic processes for the direct synthesis of dimethyl carbonate from CO_2 and methanol: A review. *Green Chem.* **2022**, *24*, 1067−1089.
(6) Honda, M.; Suzuki, A.; Noorjahan, B.; Fujimoto, K.-I.; Suzuki, K.; Tomishige, K. Low pressure CO_2 to dimethyl carbonate by the reaction with methanol promoted by acetonitrile hydration. *Chem. Commun.* **2009**, 4596−4598.
(7) Tomishige, K.; Tamura, M.; Nakagawa, Y. CO_2 conversion with alcohols and amines into carbonates, ureas, and carbamates over CeO_2 catalyst in the presence and absence of 2-cyanopyridine. *Chem. Rec.* **2019**, *19*, 1354−1379.
(8) Zhang, S.; Xia, Z.; Zou, Y.; Cao, F.; Liu, Y.; Ma, Y.; Qu, Y. Interfacial frustrated Lewis pairs of CeO_2 activate CO_2 for selective tandem transformation of olefins and CO_2 into cyclic carbonates. *J. Am. Chem. Soc.* **2019**, *141*, 11353−11357.
(9) Gong, Z.-J.; Li, Y.-R.; Wu, H.-L.; Lin, S. D.; Yu, W.-Y. Direct copolymerization of carbon dioxide and 1, 4-butanediol enhanced by ceria nanorod catalyst. *Appl. Catal., B* **2020**, *265*, No. 118524.
(10) Tian, L.; Tan, Z.; Wang, Q.; Liao, Y.-S.; Chou, J.-P.; Wu, J.-M.; Liu, G.; Peng, Y.-K. Cerium coordination-dependent surface intermediates regulate activity in dimethyl carbonate synthesis from CO_2 and methanol. *Appl. Catal., B* **2023**, *336*, No. 122914.
(11) Liu, B.; Li, C.; Zhang, G.; Yao, X.; Chuang, S. S.; Li, Z. Oxygen vacancy promoting dimethyl carbonate synthesis from CO_2 and methanol over Zr-doped CeO_2 nanorods. *ACS Catal.* **2018**, *8*, 10446−10456.
(12) Fu, Z.; Zhong, Y.; Yu, Y.; Long, L.; Xiao, M.; Han, D.; Wang, S.; Meng, Y. TiO_2-doped CeO_2 nanorod catalyst for direct conversion of CO_2 and CH_3OH to dimethyl carbonate: catalytic performance and kinetic study. *ACS Omega* **2018**, *3*, 198−207.
(13) Luo, M.; Qin, T.; Liu, Q.; Yang, Z.; Wang, F.; Li, H. Novel Fe-modified CeO_2 nanorod catalyst for the dimethyl carbonate formation from CO_2 and methanol. *ChemCatChem* **2022**, *14*, No. e202200253.
(14) Al-Darwish, J.; Senter, M.; Lawson, S.; Rezaei, F.; Rownaghi, A. A. Ceria nanostructured catalysts for conversion of methanol and carbon dioxide to dimethyl carbonate. *Catal. Today* **2020**, *350*, 120−126.
(15) Stoian, D.; Medina, F.; Urakawa, A. Improving the Stability of CeO_2 Catalyst by Rare Earth Metal Promotion and Molecular Insights in the Dimethyl Carbonate Synthesis from CO_2 and Methanol with 2-Cyanopyridine. *ACS Catal.* **2018**, *8*, 3181−3193.
(16) Giram, G. G.; Bokade, V. V.; Darbha, S. Direct synthesis of diethyl carbonate from ethanol and carbon dioxide over ceria catalysts. *New J. Chem.* **2018**, *42*, 17546−17552.
(17) Vogt, C.; Weckhuysen, B. M. The concept of active site in heterogeneous catalysis. *Nat. Rev. Chem.* **2022**, *6*, 89−111.
(18) Akbashev, A. R. Electrocatalysis goes nuts. *ACS Catal.* **2022**, *12*, 4296−4301.
(19) Tian, L.; Liao, Y.-S.; Chou, J.-P.; Tan, Z.; Chen, J. L.; Lee, J.-H.; Lo, T. W. B.; Peng, Y.-K. Facet-dependent peroxo species regulate product distribution and H_2O_2 utilization in CeO_2-catalyzed aniline oxidation. *J. Mater. Chem. A* **2023**, *11*, 14034−14042.
(20) Yuan, B.; Tan, Z.; Guo, Q.; Shen, X.; Zhao, C.; Chen, J. L.; Peng, Y.-K. Regulating the H_2O_2 activation pathway on a well-defined CeO_2 nanozyme allows the entire steering of its specificity between associated enzymatic reactions. *ACS Nano* **2023**, *17*, 17383−17393.
(21) Cheng, T.; Wu, X.; Qiu, Y.; Yuan, B.; Zhao, C.; Chen, J. L.; Peng, Y. K. Spatially decoupled H_2O_2 activation pathways and multi-enzyme activities in rod-shaped CeO_2 with implications for facet distribution. *Small* **2024**, *20*, No. e2401032.
(22) Tan, Z.; Zhang, J.; Chen, Y.-C.; Chou, J.-P.; Peng, Y.-K. Unravelling the role of structural geometry and chemical state of well-defined oxygen vacancies on pristine CeO_2 for H_2O_2 activation. *J. Phys. Chem. Lett.* **2020**, *11*, 5390−5396.
(23) Gupta, N. N.; Punekar, A. S.; EK Raj, K. R.; Ghodekar, M. M.; Patil, V. S.; Gopinath, C. S.; Raja, T. Phase transfer ceria-supported nanocatalyst for nitrile hydration reaction. *ACS Omega* **2019**, *4*, 16037−16044.
(24) Tamura, M.; Satsuma, A.; Shimizu, K.-I. CeO_2-catalyzed nitrile hydration to amide: reaction mechanism and active sites. *Catal. Sci. Technol.* **2013**, *3*, 1386−1393.
(25) Feng, X.; Sayle, D. C.; Wang, Z. L.; Paras, M. S.; Santora, B.; Sutorik, A. C.; Sayle, T. X.; Yang, Y.; Ding, Y.; Wang, X.; Her, Y.-S. Converting ceria polyhedral nanoparticles into single-crystal nanospheres. *Science* **2006**, *312*, 1504−1508.
(26) Tan, J. P. Y.; Tan, H. R.; Boothroyd, C.; Foo, Y. L.; He, C. B.; Lin, M. Three-dimensional structure of CeO_2 nanocrystals. *J. Phys. Chem. C.* **2011**, *115*, 3544−3551.
(27) Wang, S.-P.; Zhou, J.-J.; Zhao, S.-Y.; Zhao, Y.-J.; Ma, X.-B. Enhancements of dimethyl carbonate synthesis from methanol and carbon dioxide: The in situ hydrolysis of 2-cyanopyridine and crystal face effect of ceria. *Chin. Chem. Lett.* **2015**, *26*, 1096−1100.
(28) Peng, Y. K.; Chou, H. L.; Edman Tsang, S. C. Differentiating surface titanium chemical states of anatase TiO_2 functionalized with various groups. *Chem. Sci.* **2018**, *9*, 2493−2500.
(29) Tan, Z.; Li, G.; Chou, H.-L.; Li, Y.; Yi, X.; Mahadi, A. H.; Zheng, A.; Edman Tsang, S. C.; Peng, Y.-K. Differentiating surface Ce Species among CeO_2 facets by solid-state NMR for catalytic correlation. *ACS Catal.* **2020**, *10*, 4003−4011.
(30) Wang, Q.; Yi, X.; Chen, Y. C.; Xiao, Y.; Zheng, A.; Chen, J. L.; Peng, Y. K. Electronic state manipulation of surface titanium activates dephosphorylation over TiO_2 near room temperature. *Angew. Chem., Int. Ed. Engl.* **2021**, *133*, 16285−16291.
(31) Sun, G.; Li, M. M.-J.; Nakagawa, K.; Li, G.; Wu, T.-S.; Peng, Y.-K. Bulk-to-nano regulation of layered metal oxide gears H_2O_2 activation pathway for its stoichiometric utilization in selective oxidation reaction. *Appl. Catal., B* **2022**, *313*, No. 121461.
(32) Peng, Y.-K.; Tsang, S.-C. E. Probe-assisted NMR: Recent progress on the surface study of crystalline metal oxides with various terminated facets. *Magnetic Resonance Letters* **2022**, *2*, 9−16.
(33) Montini, T.; Melchionna, M.; Monai, M.; Fornasiero, P. Fundamentals and catalytic applications of CeO_2-based materials. *Chem. Rev.* **2016**, *116*, 5987−6041.
(34) Trovarelli, A.; Llorca, J. Ceria catalysts at nanoscale: how do crystal shapes shape catalysis? *ACS Catal.* **2017**, *7*, 4716−4735.
(35) Peng, Y.-K.; Fu, Y.; Zhang, L.; Teixeira, I. F.; Ye, L.; He, H.; Tsang, S. C. E. Probe-molecule-assisted NMR spectroscopy: a comparison with photoluminescence and electron paramagnetic

resonance spectroscopy as a characterization tool in facet-specific photocatalysis. *ChemCatChem* **2017**, *9*, 155−160.
(36) Frankcombe, T. J.; Liu, Y. Interpretation of oxygen 1s X-ray photoelectron spectroscopy of ZnO. *Chem. Mater.* **2023**, *35*, 5468−5474.
(37) Loridant, S. Raman spectroscopy as a powerful tool to characterize ceria-based catalysts. *Catal. Today* **2021**, *373*, 98−111.
(38) Tamura, M.; Kishi, R.; Nakayama, A.; Nakagawa, Y.; Hasegawa, J.-Y.; Tomishige, K. Formation of a new, strongly basic nitrogen anion by metal oxide modification. *J. Am. Chem. Soc.* **2017**, *139*, 11857−11867.
(39) Sawabe, K.; Yoshikawa, Y.; Satsuma, A. Density-functional theoretical study on the role of Lewis and Brønsted acid sites on CeO_2(110) surfaces for nitrile hydration. *Top. Catal.* **2014**, *57*, 1094−1102.
(40) Deringer, V. L.; Tchougréeff, A. L.; Dronskowski, R. Crystal orbital Hamilton population (COHP) analysis as projected from plane-wave basis sets. *J. Phys. Chem. A* **2011**, *115*, 5461−5466.
(41) Honda, M.; Kuno, S.; Begum, N.; Fujimoto, K.-I.; Suzuki, K.; Nakagawa, Y.; Tomishige, K. Catalytic synthesis of dialkyl carbonate from low pressure CO_2 and alcohols combined with acetonitrile hydration catalyzed by CeO_2. *Appl. Catal., A* **2010**, *384*, 165−170.
(42) Honda, M.; Kuno, S.; Sonehara, S.; Fujimoto, K.-I.; Suzuki, K.; Nakagawa, Y.; Tomishige, K. Tandem carboxylation-hydration reaction system from methanol, CO_2 and benzonitrile to dimethyl carbonate and benzamide catalyzed by CeO_2. *ChemCatChem* **2011**, *3*, 365−370.
(43) Honda, M.; Tamura, M.; Nakagawa, Y.; Nakao, K.; Suzuki, K.; Tomishige, K. Organic carbonate synthesis from CO_2 and alcohol over CeO_2 with 2-cyanopyridine: scope and mechanistic studies. *J. Catal.* **2014**, *318*, 95−107.
(44) Unnikrishnan, P.; Darbha, S. Direct synthesis of dimethyl carbonate from CO_2 and methanol over CeO_2 catalysts of different morphologies. *J. Chem. Sci.* **2016**, *128*, 957−965.
(45) Wang, S.; Zhou, J.; Zhao, S.; Zhao, Y.; Ma, X. Enhancement of dimethyl carbonate synthesis with in situ hydrolysis of 2, 2-dimethoxy propane. *Chem. Eng. Technol.* **2016**, *39*, 723−729.
(46) Kresse, G.; Furthmüller, J. Efficient iterative schemes for ab initio total-energy calculations using a plane-wave basis set. *Phys. Rev. B* **1996**, *54*, 11169.
(47) Blöchl, P. E. Projector augmented-wave method. *Phys. Rev. B* **1994**, *50*, 17953.
(48) Kresse, G.; Joubert, D. From ultrasoft pseudopotentials to the projector augmented-wave method. *Phys. Rev. B* **1999**, *59*, 1758.
(49) Perdew, J. P.; Burke, K.; Ernzerhof, M. Generalized gradient approximation made simple. *Phys. Rev. Lett.* **1996**, *77*, 3865.
(50) Dudarev, S. L.; Botton, G. A.; Savrasov, S. Y.; Humphreys, C.; Sutton, A. P. Electron-energy-loss spectra and the structural stability of nickel oxide: An LSDA+ U study. *Phys. Rev. B* **1998**, *57*, 1505.

https://doi.org/10.1021/acscatal.4c04639
ACS Catal. 2024, 14, 16861−16871